Energy & Environmental Science

ROYAL SOCIETY OF CHEMISTRY

PAPER

View Article Online
View Journal | View Issue

Cite this: *Energy Environ. Sci.*, 2025, **18**, 9611

Unveiling capacity limitations of MnO_2 in rechargeable Zn chemistry

Cheng Liu, [a] Vlad Martin-Diaconescu, [b] Ashley Phillip Black, [a] Siavash Khabazian, [a] Bernat Mundet, [c] Krzysztof Matlak, [d] Lorenzo Stievano, [ef] Andrea Sorrentino, [b] Laura Simonelli *[b] and Dino Tonti *[a]

Received 25th June 2025,
Accepted 26th September 2025

DOI: 10.1039/d5ee03588k

rsc.li/ees

Aqueous Zn–MnO_2 batteries with mildly acidic electrolytes deliver attractive experimental capacities, however the underlying mechanisms remain elusive, particularly regarding the interactions of Zn^{2+} and H^+ with MnO_2, as well as the formation of Mn^{2+} and $Zn_4SO_4(OH)_6{\cdot}xH_2O$ (ZSH). Although these products are compatible with a two-electron dissolution mechanism, the observed first-discharge capacity is limited to approximately 300 mA h g^{-1} MnO_2, close to that of a one-electron reaction. To address this contradiction, commonly used α-MnO_2 nanowires were chosen as cathode material and investigated by a systematic multimodal and multiscale approach under *operando* or *ex situ* conditions to analyze the processes that occur during the first discharge. MnO_2 dissolution into Mn^{2+} and ZSH precipitation were confirmed, and the formation of a disordered phase at the nanowire surface with the accumulation of Mn(III) was detected. An in-depth analysis indicates that such Mn(III) species correspond to protonated corner-sharing MnO_2 octahedra, which, unlike the edge-sharing ones, are hindered from undergoing disproportion, limiting the MnO_2 dissolution and explaining the reduced capacity. This comprehensive mechanistic understanding opens new pathways for the selection of the most appropriate MnO_2 phases and the optimization of electrodes to improve the performance of aqueous Zn–MnO_2 battery systems.

Broader context

A safe and sustainable energy storage system is essential for achieving Net Zero Emissions by 2050. Thanks to the inherent safety, energy density comparable to lithium-ion chemistry, and low cost, rechargeable mildly acidic aqueous zinc–manganese dioxide (Zn–MnO_2) chemistry is drawing increasing interest. However, while encouraging performance has been repeatedly reported, several contradictory mechanisms have been proposed. Notably, a contradiction persists between the specific capacity and the most accepted mechanism. In fact, while a 2-electron MnO_2 dissolution into soluble Mn^{2+} has been shown by several authors, the experimental 1st discharge capacities are usually close to the equivalent 1 electron. Using multiple spectroscopy and microscopy techniques, we verify that while the 2-electron mechanism is correct, a peculiar passivation effect builds up during discharge, involving the accumulation of Mn–Mn configurations that hinder the second step, the disproportionation of Mn(III) requiring a fast charge transfer between Mn centers. Understanding this essential problem unlocks the perspectives for a more comprehensive control of the electrode chemistry and the design of more efficient Zn–MnO_2 batteries.

[a] *Institut de Ciència de Materials de Barcelona, Consejo Superior de Investigaciones Científicas (ICMAB-CSIC), Carrer dels Til·lers sn, 08193 Bellaterra, Spain. E-mail: chengliu@icmab.es, ablack@icmab.es, skhabazian@icmab.es, dino.t@csic.es*

[b] *ALBA Synchrotron Light Source, 08290 Cerdanyola del Vallès, Barcelona, Spain. E-mail: vmartind@cells.es, asorrentino@cells.es, lsimonelli@cells.es*

[c] *Catalan Institute of Nanoscience and Nanotechnology (ICN2), CSIC and BIST, Campus de la Universitat Autònoma de Barcelona (UAB), Barcelona, Bellaterra, 08193, Spain. E-mail: bernat.mundet@icn2.cat*

[d] *SOLARIS National Synchrotron Radiation Centre, Czerwone Maki 98, 30-392 Kraków, Poland. E-mail: krzysztof.matlak@uj.edu.pl*

[e] *Institut Charles Gerhardt Montpellier (ICGM), Univ. Montpellier, CNRS, ENSCM, 34293 Montpellier, France*

[f] *Réseau sur le Stockage Electrochimique de l'Energie (RS2E), CNRS, 80039 Amiens, France. E-mail: lorenzo.stievano@umontpellier.fr*

Introduction

A carbon-neutral society requires safe and sustainable energy storage technologies that overcome the limitations of current Li-ion batteries.[1,2] One of the most promising options is rechargeable aqueous zinc manganese dioxide (Zn–MnO_2) chemistry. Indeed, the Zn abundance, quick response, non-flammable nature of the electrolyte, and high theoretical specific capacity provided by both electrodes (respectively 616 mA h $g^{-1}_{MnO_2}$, based on a $2e^-$ reaction, and 820 mA h g^{-1}_{Zn})[3–6] make them attractive for energy storage purposes. Although research on neutral Zn–MnO_2 batteries began over 30 years ago,[7] stable performance at large areal capacities and wide

current ranges has not been demonstrated consistently, and significant aspects of the mechanism remain unclear.[8,9] Understanding the evolution and degradation of MnO_2 cathodes in a typical mildly acidic aqueous electrolyte still remains challenging,[8,10] because of the intrinsic system complexity, arising from multiple equilibria and the formation of poorly crystalline phases with several coexisting Mn redox states.[11,12]

Assuming a straightforward transition from $Mn^{IV}O_2$ to Mn(III)-based species in the cathode, a Zn intercalation/deintercalation mechanism has been initially proposed.[13–16] This process in aqueous Zn and Mn electrolytes would produce Zn–Mn compounds during cycling, which have been occasionally observed *ex situ* by weak X-ray diffraction (XRD) signals.[13–18] Instead, the more frequent observations of zinc hydroxysulfates, ($Zn_4SO_4(OH)_6{\cdot}xH_2O$, ZSH) formation, suggested conversion or insertion reactions involving protons (H^+), along with the formation of MnOOH, "$HMnO_2$" or dissolved Mn species.[19–22] Within this pathway, the formation of ZSH acts as a buffer to hinder pH increase and stabilize local pH fluctuations.[23–25] Consistently with this picture, Mn^{2+} dissolution in aqueous Zn^{2+} electrolytes has been frequently reported.[13,24,26,27] The most common explanation is that high-spin Mn(III)-based species are inherently unstable and affected by Jahn–Teller distortions, inducing disproportionation into $Mn^{IV}O_2$ and aqueous Mn^{2+}.[13] However, Mn(III), expected as intercalation product or as intermediate for a two-step reduction has proven quite elusive. Although previous studies have reported various Mn(III) species using *ex situ* characterization under ambient conditions,[15,26,28,29] bulk-sensitive *operando* data cannot detect them.

Several *operando* techniques, such as X-ray absorption spectroscopy (XAS),[30,31] electron spin resonance (ESR),[32] X-ray fluorescence spectroscopy (XRF),[33] and Raman,[34] indicate a dissolution/redeposition of MnO_2 involving a two-electron reaction, with $Mn^{IV}O_2$ conversion to Mn^{2+}, which then diffuses into the electrolyte. Despite this evidence, the vast majority of studies on chemically prepared MnO_2 report scattered values of experimentally delivered capacities despite the limited number of reaction paths, with a maximum delivered capacity typically confined below 350 mA h $g^{-1}_{MnO_2}$[29,35–43](closer to $1e^-$ reaction) during the first discharge. Instead, the usual addition of Mn^{2+} to the initial electrolyte to moderate dissolution can artificially enhance the electrode capacity during cycling. The underlying cause of this contradiction between experimental capacity and the generally accepted 2-electron mechanism remains unclear.

Herein, this inconsistency was investigated using a combination of *operando* and *ex situ* techniques and data analysis methods. *Operando* bulk sensitive XRD and XAS confirmed the main mechanism of α-MnO_2 dissolution into soluble Mn^{2+} with ZSH formation. However, *ex situ* soft X-ray transmission microscopy (TXM), scanning transmission electron microscopy-electron energy loss spectroscopy (STEM-EELS), and Mn X-ray emission spectroscopy (XES) revealed an increased presence of a Mn(III) minority phase on the remaining MnO_2 nanowire surfaces after discharge. Interestingly, the extended X-ray absorption fine structure (EXAFS) analysis allowed us to identify a decreased ratio of $Mn–Mn_{edge}$ *vs.* $Mn–Mn_{corner}$ contribution in the discharge with respect to the pristine state, indicating that $Mn–Mn_{edge}$ sites are the ones which dissolve along discharge into the electrolyte, where their unavailability at the surface seems to be the cause that terminates the $2e^-$ process before all α-MnO_2 is removed.

Results and discussion

Capacity limitations

Several electrodes based on the synthesized α-MnO_2 active material were tested in standard $ZnSO_4$ electrolytes with $MnSO_4$ additive. The concentrations of $ZnSO_4$ and $MnSO_4$ additive in the electrolyte and the loading of the α-MnO_2 in the cathode at the pristine state were chosen as a compromise between common electrochemical conditions reported in the literature (*e.g.* for optimal Zn cycling[44] and MnO_2 stability[19,45,46]) and the absorption ranges required for optimal spectroscopic signal quality of *operando* XAS. As depicted in Fig. S5, the effect of Zn and Mn salt concentrations in the electrolyte is modest. To understand the extent to which electron conductivity or ion diffusion influences the experimental capacity, the electrode mass loadings and carbon content were varied. As shown in Fig. 1(a), while the experimental capacity shows different trends depending on the electrode formulation, it remains limited to *ca.* 350 mA h $g^{-1}_{MnO_2}$. A lower current did not lead to a substantial increase in capacity (Fig. 1(b)). Possible modifications in the electrolyte composition during cycling were ruled out, because the capacity was not extended by refreshing the electrolyte after discharge or using a significantly larger volume, suggesting that the discharge capacity is intrinsically related to the active material itself.

The relatively low capacity could be attributed to some limiting mechanisms, or to a simple one-electron reduction from $Mn^{IV}O_2$ to Mn(III) species. However, Mn(III) as the main oxidation state at the end of discharge should be ruled out based on abundant previous literature,[30,47–52] and on the results reported below. Nevertheless, discharge in an organic aprotic electrolyte delivered only a small capacity (Fig. S4), confirming the involvement of protons in the mechanism.

From another perspective, *operando* XRD data indicated that incomplete MnO_2 dissolution was observed at the end of the first discharge (Fig. S16). Admitting a 2-electron mechanism leading to Mn^{2+}, a passivation of MnO_2 could prevent its complete dissolution. In the past, ZSH formation was suggested to block Mn dissolution.[46] We carefully analyzed the details of the α-MnO_2 surface by TEM. The STEM-HAADF images in Fig. 1(c), (d) and Fig. S6 show evident lattice planes at the surface of pristine α-MnO_2. In contrast, the surface of the discharged material was amorphous and irregular. The Mn, K, and Zn distributions in the discharged state obtained by TEM-EDX are shown in Fig. 5(e) and (f). The images show similar Mn and K distributions. Instead, Mn and Zn do not coexist (Fig. S7 and S8), confirming the absence of any Zn intercalation in the α-MnO_2 structure. Remarkably, Zn is

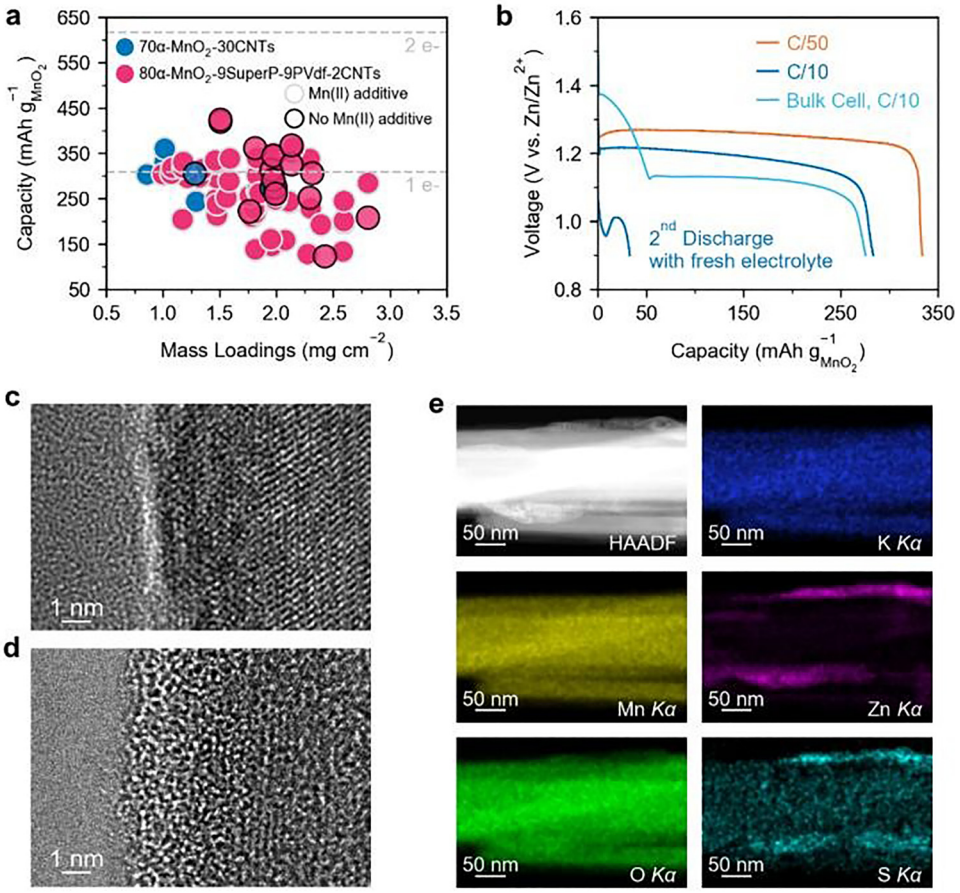

Fig. 1 First discharge capacities obtained from several cells using cathodes of different conductivities and mass loadings, with and without the $MnSO_4$ additive (a). Additional attempts to enhance the capacity of α-MnO_2 with low C rate (C/50), excess electrolyte (bulk cell), and refreshing electrolyte (C/10) (b). STEM-HAADF images of pristine (c), and the discharged (d) electrodes. TEM-EDX maps of K, Mn, Zn, S, and O elements in the discharged sample (e).

essentially segregated at the surface. However, as shown in Fig. S9 and Table S5 within the Zn layer, we found a S : Zn atomic ratio of 0.076 ± 0.009, far from the value expected for ZSH (*ca.* 0.25), whereas the Zn : O ratio was close to 1 : 1, which is compatible with ZnO. The formation of ZnO could be favored by a local increase in pH, which is associated with MnO_2 protonation. To prove the specific role of pH and the presence of Zn species in the electrolyte, the same electrode was discharged in Zn-free, large-volume cells (Fig. S10). As reported in previous studies,[49] the pH modulates the discharge potential, but we observe that capacities are only slightly affected by the presence of Zn. Since localized pH close to the surface of α-MnO_2 cathode is challenging to measure, we stabilized pH by using a bulk electrolytic cell with electrolyte buffered at pH 5.0 and 2.0 and under stirring, to minimize composition gradients (Fig. S11). Particularly at pH 2.0, ZSH or ZnO formation should be suppressed.[53–55] Nevertheless, we observed again similar capacities as in the thin-electrolyte cells. This rules out pH or cell geometry as responsible for the capacity limitation. A possible passivating role of ZnO, leading to incomplete MnO_2 dissolution and limitation of the discharge capacity, seems unlikely.

Mn oxidation state in pristine α-MnO_2

Since Zn in the environment did not demonstrate a key role in the discharge mechanism, we focused on the analysis of the Mn active material itself. A more accurate estimation of the expected capacity should be based on the pristine oxidation state of Mn. The K : Mn atomic ratio determined by Inductively coupled plasma-optical emission spectrometry (ICP-OES) was 0.107 ± 0.003, which corresponds to a Mn oxidation state in pristine α-MnO_2 of 3.893 ± 0.003, assuming the formation of stoichiometric Mn : O = 1 : 2 and no oxygen vacancies (Table S6).

The energy position of the first-derivative maximum of the bulk-sensitive Mn K-edge X-ray absorption near edge structure (XANES) corresponds to an average Mn oxidation state of 3.89 ± 0.05 (Fig. S12),[16] which is in excellent agreement with this value. Compatible results were obtained by fitting the XANES pre-edge features with the corresponding $Mn^{IV}O_2$, $Mn^{III}{}_2O_3$, and Mn^{II} (aq.) references (Fig. 3(c) and Table S2). Moreover, TEM-EDX showed a K : Mn atomic ratio of 0.082 ± 0.006, corresponding to a Mn oxidation state of 3.92 ± 0.01 (Fig. S13 and Table S7), where the minor quantitative discrepancy probably depends on the limited region probed. Both TXM cluster analysis and onset energy analysis of the STEM-

EELS data showed an evident Mn energy shift towards low energies on the α-MnO_2 nanowire surface, implying an accumulation of Mn(III) species there (Fig. S14), in agreement with the XPS data showing a high Mn(III)/Mn(IV) surface ratio, close to 1 (Fig. S15).[56] Considering an experimental initial Mn oxidation state of +3.89 allows a more accurate estimation of the theoretical capacity, resulting in 263 and 557 mA h $g^{-1}_{MnO_2}$ from the exchange of 1 or 2 electrons, respectively. From the same initial value, after a discharge of 350 mA h $g^{-1}_{MnO_2}$, an average Mn oxidation state of +2.7 would be expected, which is much smaller than that reported in the following, supporting again the substantial Mn dissolution mechanism rather than simply Zn or H intercalation in α-MnO_2, which should instead lead to Mn(III) in the discharged electrode.

Direct observation of α-MnO_2 dissolution

Operando XRD and XAS measurements were carried out to follow the evolution of the main species involved along the first discharge. The evolution of the XRD patterns is shown in Fig. S16. During discharge, the intensity of the α-MnO_2 reflections rapidly decrease compared with that of the Ti foil reference. Meanwhile, ZSH continuously forms as the process progresses. However, a few new weak peaks, possibly matching defective MnO_2 with formula $K_{0.66}Mn_4O_8$ appear (Fig. S17), while incomplete α-MnO_2 dissolution is observed. *Operando* Mn and Zn K-edge XAS data were acquired quasi-simultaneously in transmission mode on coin cells with Kapton windows, with the cells assembled such that both the cathode and electrolyte regions could be probed (Fig. 2(c)). The electrolyte composition utilized was 0.5 M $ZnSO_4$ and 0.2 M $MnSO_4$, and the electrode loading *ca.* 2.12 mg cm^{-2} to optimize the XAS signal. The possible effect of the X-ray beam on the studied system was characterized and suppressed prior to the *operando* measurements by unfocusing and attenuating the incoming beam. The spectra at the exposed point at the end of the discharge overlapped with those collected at a freshly irradiated point in the same state of charge, whereas the delivered capacity along the first discharge was 275 mA h $g^{-1}_{MnO_2}$, comparable to typical laboratory experiments (Fig. S18), validating the representativeness of the reported results.

Mn and Zn K-edge XANES evolutions along the first discharge, carrying out information on the Mn and Zn oxidation state and local environment,[57,58] are presented in Fig. 2(a) and (b), respectively. The intensity of the signal related to dissolved Mn^{2+} (aq.) continuously increased during discharge at the expense of α-MnO_2, evidencing a few isosbestic points, indicating direct conversion without intermediates. Similarly, the Zn^{2+} (aq.) signal decreased, whereas the ZSH signal increased during discharge, also showing few isosbestic points. In both cases, the electrolyte signals remained unaltered during the entire discharge process, indicating that no additional soluble Mn or Zn species were formed (Fig. S19).

The evolution of Mn and Zn species was quantified by LCF with respect to the electrolyte and α-MnO_2 or ZSH references, respectively, and confirmed by advanced statistical methods (PCA and MCR-ALS analyses). Indeed, the PCA of the *operando* Mn and Zn K-edge spectra collected during discharge identified two components, which were then reconstructed using MCR-ALS (Fig. S20). Both LCF and MCR-ALS reliably reproduced the experimental datasets, with consistent results between the two

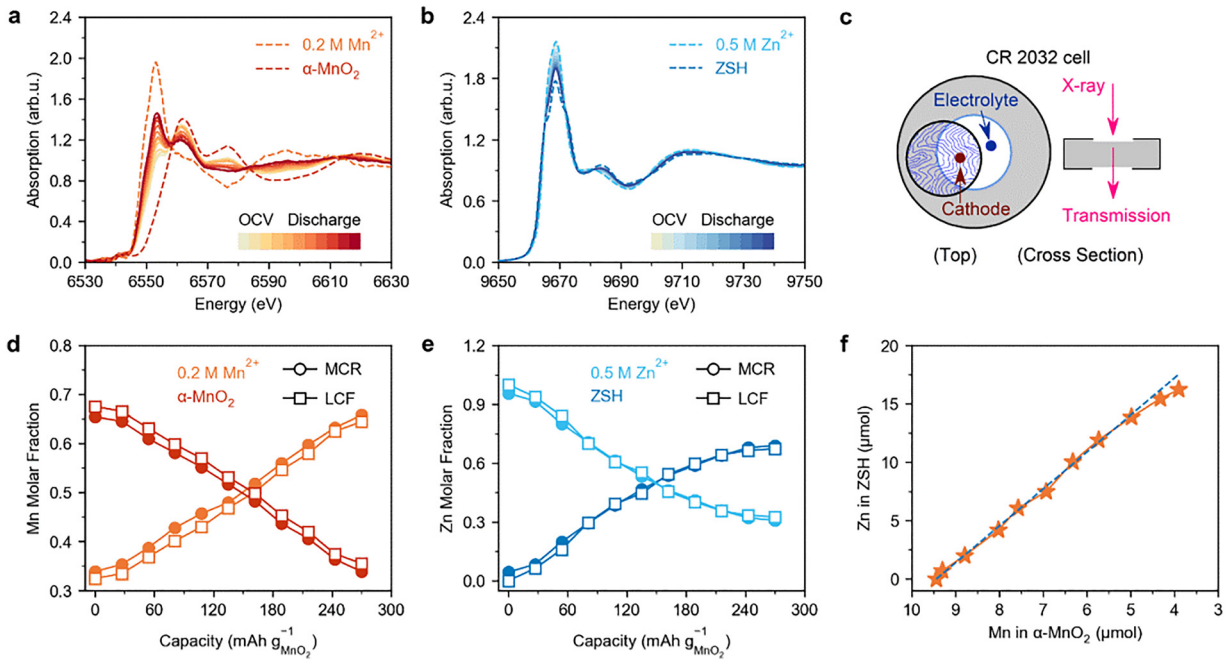

Fig. 2 *Operando* XANES at the Mn (a) and Zn (b) K-edge on α-MnO_2 cathode. The LCF fitting and statistical MCR-ALS results were compared for both the Mn (d) and Zn (e) K-edges. Sketch of the experimental geometry used to acquire *operando* XAS (c). Correlation of absolute Zn and Mn amounts in the cell based on the edge jump of *operando* XAS (f).

approaches. Moreover, the evolution of the Mn and Zn absorption jumps for the spectra collected on the electrolyte and cathode allowed the determination of the electrolyte Mn and Zn concentrations and the actual amounts of MnO_2 and ZSH species present in the cathode during the measurement. The calculation details are reported in SI Part I. For the Mn K-edge (Fig. 2(d)), the molar fractions of the two Mn components varied linearly with capacity. Deviations from linearity were observed in the evolution of Zn species (Fig. 2(e)), with a clear saturation effect at the end of the discharge owing to Zn^{2+} formed from anode dissolution. The quantitative correlation between Zn in ZSH and Mn in MnO_2 form (Fig. 2(f)) instead remained almost linear throughout the process, with only a small deviation at the end of discharge. This confirms that α-MnO_2 dissolution and ZSH formation are the main processes occurring during discharge. The deviation from linearity for the last points indicates that the ZSH formation rate decreases with respect to Mn dissolution towards the end of the discharge. This may be related to the previously described presence of ZnO, which may form preferentially in these later stages.

To explore the dissolution from the point of view of the local structure, Fourier transforms (FTs) of *operando* Mn and Zn K-edge EXAFS spectra are shown in Fig. 3(a) and (b). Absence of peaks at the same radial distance in the Mn and Zn K-edge FTs exclude the formation under discharge of Zn–Mn mixed-phases. Indeed, at the Zn K-edge, the features at approximately 1.58 and 2.68 Å correspond to the contribution from Zn–O (first shell for the Zn^{2+} (aq.) and ZSH phases) and Zn–Zn (second shell of the ZSH phase), respectively. At the Mn K-edge the features at around 1.45, 1.83, 2.42, and 3.00 Å, correspond respectively to contributions from the Mn–O (first shell for the α-MnO_2 phase), Mn–O (first shell for the Mn^{2+} (aq.) phase), Mn–Mn_{edge} (second shell with edge-sharing octahedra for the α-MnO_2 phase), and Mn–Mn_{corner} (second shell with corner-sharing octahedra for the α-MnO_2 phase), as shown in Fig. S21–S23, and Table S8. The changes in the intensities of the Zn and Mn radial distributions correspond to the decrease/increase in the corresponding phase content as the discharge progresses.

The erosion and fragmentation of the pristine α-MnO_2 nanowires is evidenced by the decrease in the Mn–O feature at 1.45 Å, whereas the ZSH deposition corresponds to the development of the Zn–Zn distance peak at 2.68 Å. Interestingly, the intensity of the Mn–Mn_{edge} contribution decreased faster than that of the Mn–Mn_{corner} (insert in Fig. 3(a)), which instead remained approximately constant, with the contribution of both peaks significantly above the noise level (Fig. S24).

To explain these results, we propose that the Mn–Mn_{corner} configuration is essentially maintained when the surface layers of the crystal are protonated and Mn reduced. As a consequence, the charge transfer implied by disproportionation can occur under these Mn–Mn_{corner} and Mn–Mn_{edge} possible configurations, but with the shorter edge-shared configuration being much more efficient. As a result, the formed Mn(II) will

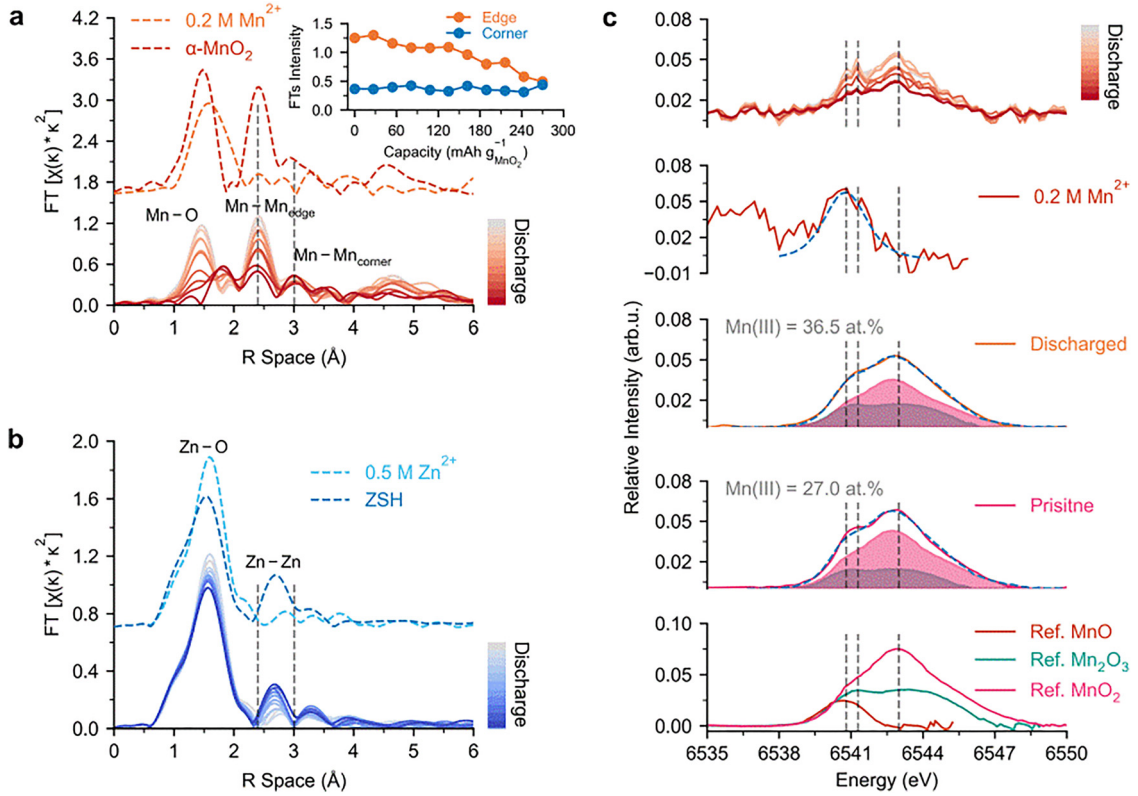

Fig. 3 FTs-EXAFS of *operando* XAS at Mn (a) and Zn (b) K-edges; the inset in (a) shows the evolution of areas measured at the 2.42, and 3.00 Å peaks. Pre-edge evolutions and fits of the pristine and discharged samples (c).

dissociate from its oxygen ligands so that the corresponding octahedron, mainly originally in the Mn–Mn_{edge} configuration, is lost. This would bring to an accumulation of inactive protonated and reduced Mn–Mn_{corner} octahedra, which would block further reactions.

Mn oxidation state in the discharged electrode

The Mn K-edge pre-peak and Mn $K_{\beta 1,3}$ XES features are sensitive to the details of the local Mn electronic properties. During discharge, the evolution of the Mn K-edge pre-peak shown in Fig. 3(c) suggests an increase in the Mn(III)/Mn(IV) ratio, whereas the *ex situ* Mn $K_{\beta 1,3}$ spectra are compatible with a minor overall increase in Mn(III) in the electrode (Fig. S25).

Complementary information was obtained at the Mn L-edge, which is usually more sensitive than the K-edge to oxidation states, and is less affected by the local coordination environment.[57] In particular, *ex situ* TXM, *in situ* Mn L_3-edge STXM and *ex situ* STEM-EELS experiments were carried out to assess the spatial distribution of the detected Mn and Zn species, where microscopy allowed the detection of inhomogeneously distributed minority species. TXM clearly shows that the nanowires in the discharged state (Fig. 4(b)) were eroded compared with the pristine ones (Fig. 4(a)), appearing broken and shrunk in both *ex situ* and *in situ* images (Fig. S26) because of the α-MnO_2 dissolution. *In situ* STXM confirmed the wire erosion and spectral changes observed by *ex situ* TXM (Fig. S26c and d). As detailed in eqn (S23), we define a shape index for the Mn L-edge spectrum as the arctangent of the absorption feature intensity ratio at energies of maximum sensitivity to Mn(III) and Mn(IV) species.[59] Thus, the shape index is directly related to the degree of contribution of Mn(III) to Mn(IV). In Fig. 4, the higher shape index distribution reflects the higher Mn(III) content on the surface of the nanowires, with an average shift towards reduced Mn after discharge, as indicated by the peak shift in the histograms (Fig. 4(c)). This is consistent with the Mn(III)-rich surface determined by *ex situ* X-Ray photoelectron spectroscopy (XPS) analysis (Fig. S27). The fact that all the distributions generally shift towards higher values of the shape index without new obvious components in the histogram indicates that no localized new phases are formed within the TXM spatial resolution (*ca.* 40 nm, half pitch). In addition, the shift is modest compared to the position of the $Mn^{III}OOH$ reference, as reduced Mn still involves a small fraction of the remaining Mn. This reduction was further confirmed by the lower onset energy of the Mn L_3 edge,[60] as shown in Fig. S28. To appreciate the variability of the spectra, image pixels were grouped within ranges of the shape index, and their L_3 edge spectra were averaged (Fig. 4(d)). The averaged Mn L_3 edge spectra clearly show the coexistence of the majority Mn(IV) with a characteristic sharp peak at 641.7 eV and a minority reduced phase. The discharged sample shows that more reduced Mn is found towards the surface of the nanowires (Fig. 4(c)). Cluster analysis of STEM-EELS showed a similar difference between the bulk and surface spectra (Fig. S28a–c). Given the minor contribution of Mn(III) in every image pixel, the spectra reported in Fig. 4(d) do not show major variations. However, the three pure components were clearly differentiated by PCA and MCR-ALS (Fig. 4(e) and Fig. S29).

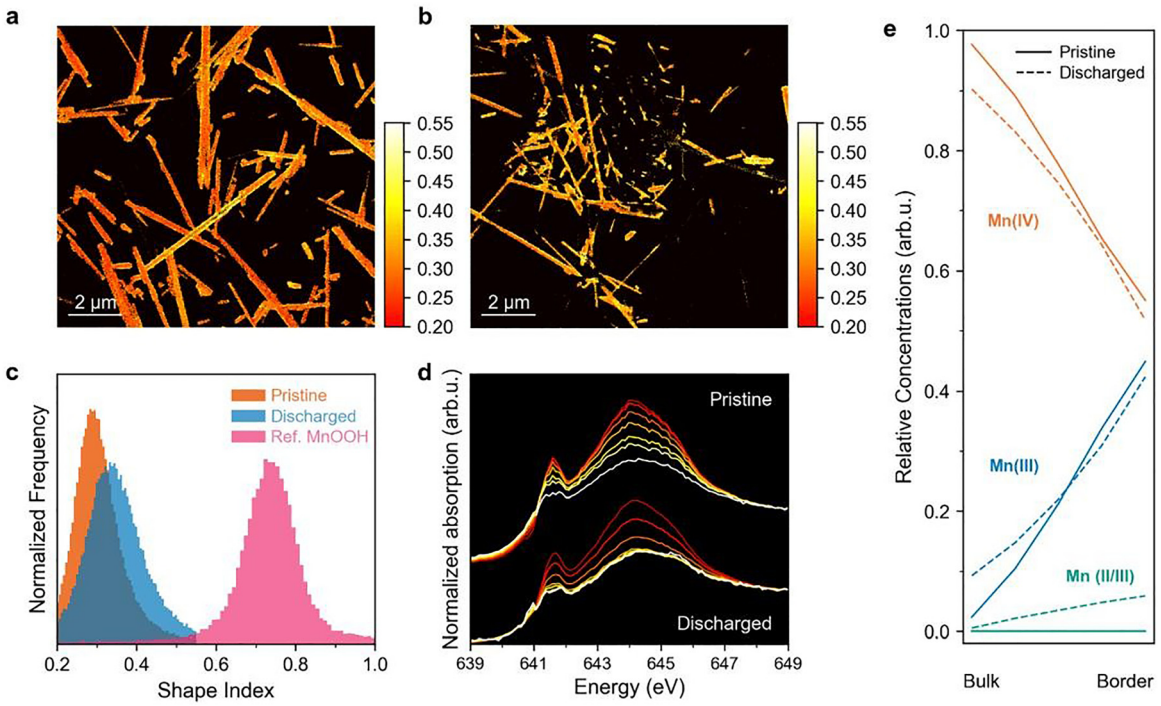

Fig. 4 Maps of shape index of the Mn L-edge, sensitive to the Mn reduction for pristine (a) and discharged (b) electrodes. Corresponding histogram (c) and average spectra for different ranges of shape index that are considered sufficiently representative of the collected pixels and used for PCA and MCR-ALS analysis (d). Relative concentrations of the calculated Mn L-edge components determined by PCA and MCR-ALS (e).

Two components are already present in the pristine sample and can be attributed to the bulk α-MnO_2 and to surface Mn, which has an increased Mn(III) character, as discussed previously. After discharge, the concentration profiles of these components remained almost unchanged. A third component only appears in the discharged sample towards the surface and corresponds to a spectrum with a threshold shifted by more than 1 eV towards lower energies and resembling Mn_3O_4.[57] This signature suggests that some of the Mn(II) formed by the disproportionation of Mn(III) may remain trapped in the solid oxide.

Finally, TEM-EDX fittings of the discharged samples indicated the same K : Mn ratio of 0.082 ± 0.006 as that of pristine α-MnO_2, suggesting that K was not preferentially dissolved or retained as α-MnO_2 was reduced (Fig. S9 and Table S7).

The cause of the capacity limitation

In summary, the reported data are compatible with protonation as the first step for the discharge reaction:[61]

$$Mn^{IV}O_2 + H^+ + e \rightarrow HMn^{III}O_2 \quad (1)$$

quickly followed by a disproportionation reaction.

$$HMn^{III}O_2 + HMn^{III}O_2 \rightarrow Mn^{IV}O_2 + Mn^{2+} + 2OH^- \quad (2)$$

We indicate as "$HMn^{III}O_2$" the Mn(III) produced by the reduction of $Mn^{IV}O_2$, not having obtained evidence of a specific compound and with the formation of a soluble Mn(III) being unlikely. Thus, Mn(III) remains solid during discharge and is converted into soluble Mn^{2+} and back to $Mn^{IV}O_2$. The increased amount of reduced Mn suggests that some Mn(III) intermediates and even Mn(II) products might remain trapped as solids in the disordered surface layer of the α-MnO_2 remnants.

It is important to stress that reaction (2) actually implies an electron transfer from one Mn(III) to another Mn(III). Based on the Mn K-edge EXAFS results, it can be proposed that only edge-sharing couples of [$Mn^{III}O_6$] octahedra are capable of efficient Mn disproportionation (Fig. 5(a)). Even if metal–metal coupling in oxides can be extremely complex,[62–64] this electron hopping seems easier for edge-sharing sites but more difficult for corner-sharing units, which are separated by a larger distance and eclipsed by the oxygen shared by both octahedra. As captured in Fig. 3(a), the dissolution process removes edge-sharing units; therefore, corner-sharing octahedra accumulate at the surface, which become richer in Mn(II/III) and amorphous species (see Fig. 5(b)). This blocks further electron transfer, deeper protonation, and/or Mn^{2+} release, thereby acting as a passivation layer.

Interestingly, the literature does report high coulombic efficiency when manganese oxide is deposited electrolytically, typically under potentiodynamic or potentiostatic charging,[47–49,65–67] To prove if a specific Mn coordination is involved in such cases, Mn oxide electrodeposited from a solution of $ZnSO_4$ and $MnSO_4$ buffered at pH 4.2 was investigated. The obtained electrodeposited MnO_2 appears disordered and nanostructured (Fig. S31), consistent with layered birnessite-MnO_2, as indicated by its comparable EXAFS features and lattice spacings in the electron

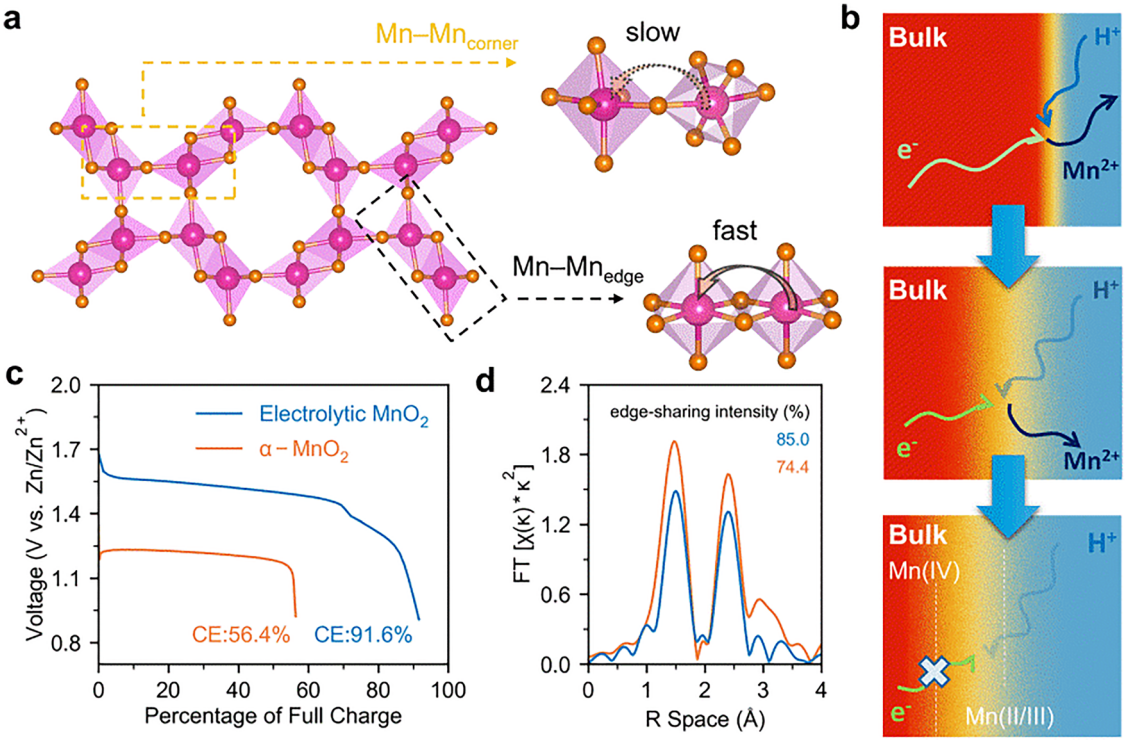

Fig. 5 Proposed mechanism for the evolution of the α-MnO_2 surface during discharge (a), scheme for the charge transfer required in the second step of MnO_2 dissolution (b), and comparison of discharges for obtained by two different MnO_2 phases with respect to the theoretical capacity. (c) and the respective FTs-EXAFS (d).

diffraction pattern.[68,69] Also in our case, we observed discharges with a coulombic efficiency above 90% (Fig. S30). The FTs-EXAFS spectrum (Fig. 5(d)) exhibits a strong peak at 2.42 Å and a very weak peak at 3.00 Å, with less than 15% corner-sharing Mn–Mn octahedra, demonstrating that the edge-sharing configuration is essential for the quantitative dissolution of MnO_2.

Conclusions

The capacity limitation and mechanism of rechargeable aqueous Zn–MnO_2 batteries were revealed using a multimodal and multiscale characterization approach. Both *operando* XAS and XRD confirm α-MnO_2 dissolution and ZSH formation during discharge. The erosion of α-MnO_2 during discharge produces disorder and accumulation of reduced Mn species at the surface of the nanowires. The substantial decline in the Mn–Mn_{edge} distances *vs.* Mn–Mn_{corner} suggests that the second reaction step, that is, Mn(III) disproportionation, requires edge-connected Mn octahedral pairs. The accumulation of corner-sharing protonated octahedra at the surface of the nanowires blocks electron and ionic exchange before α-MnO_2 complete dissolution. Given that capacity limitation is observed to different extents with most MnO_2 polymorphs,[61] corner-sharing Mn in the pristine structure could be not the only factor limiting the capacity. The here reported results suggest that efficient electron and ion conduction paths in the active cathode material should persist during discharge. Short diffusion paths, as typically present in nanostructured particles,[42,70] or doping,[71–74] should effectively contribute to an optimal discharge. However, nanostructuring,[75–77] or doping[38,78,79] alone do not seem generally sufficient for quantitative MnO_2 dissolution. Instead, generally high reversibility is observed with MnO_2 phases electrodeposited during charge. These typically offer faster ion/electron transfer that originates from porous nanostructured and defective layered phases,[80] for which the isolation of corner–corner configurations should be less likely, and short ion diffusion paths are expected.

Experimental

Materials synthesis

α-MnO_2 nanowire was prepared *via* a standard hydrothermal method.[26] Briefly, 3.5 mmol potassium chlorate ($KClO_3$, 99 + % ACS Reagent, Thermos Scientific), 2 mmol manganese(II) sulfate monohydrate ($MnSO_4{\cdot}H_2O$, 99%, Labkem), and 3.5 mmol potassium acetate (CH_3COOK, 99%, Thermos Scientific) were dissolved in 30 mL Milli-Q water. After adding 1.6 mL of glacial acetic acid (EssentQ, Scharlab) was added and stirred for half an hour, and the homogeneous solution was transferred into a Teflon-lined autoclave (50 mL, Canrd) and maintained at 160 °C for 12 h. Finally, the as-synthesized sample was filtered under vacuum using Milli-Q water/ethanol and then dried at 60 °C overnight. The α-MnO_2 nanowire powder had a single-phase tetragonal structure (*I*4/*m*, PDF#00-044-0141, $K_{1.33}Mn_8O_{16}$), which consisted of a typical 1 × 2 [MnO_6] tunneled framework with K^+ ions partially occupying the tunnel center (Fig. S2).[81] Transmission electron microscopy energy-dispersive X-ray spectroscopy (TEM-EDX) and HRTEM confirmed that potassium had a uniform distribution in the structure (Fig. S3).

Electrochemical measurements

Binder-free MnO_2 electrodes were prepared using α-MnO_2 nanowires and multiwall carbon nanotubes (MWCNT) with a mass ratio of 7 : 3. The normal cathode was obtained using α-MnO_2 nanowire, carbon black (Super P, Timcal), polyvinylidene fluoride (PVdF, Sigma-Aldrich), and multiwall carbon nanotubes (MWCNT) with a weight ratio of 80 : 9 : 9 : 2. The mass loading of the α-MnO_2 electrodes was *ca.* 0.8–2.5 mg cm^{-2}. Electrochemical Swagelok cells were assembled with cathodes, glass fiber separators (thickness, 270 mm, PRAT-DUMAS), zinc foils (thickness, 0.125 mm, Advent Research-Materials), and different aqueous electrolytes: 1 M $ZnSO_4$ with 0.2 M $MnSO_4$, and 1 M $ZnSO_4$. To minimize the effects of the limited electrolyte volume, 40 mL homemade bulk cells were also used with α-MnO_2 cathodes and Zn foils or carbon paper as anodes, both with an area of 3 cm^2 in various aqueous liquid electrolytes: 1 M $ZnSO_4$ + 0.2 M $MnSO_4$, 1 M Na_2SO_4 + 0.2 M $MnSO_4$, or 1 M $ZnSO_4$ + 0.2 M $MnSO_4$ supplemented with various buffered agents, including 0.1 M potassium acetate with acetic acid (pH at 5.0), H_2SO_4 (pH at 2.0), and 1 M acetic acid adjusted with ammonia (pH at 4.2). The configurations of the *in situ* coin cells for *operando* XRD and XAS were similar to those of the Swagelok cells, but 0.5 M $ZnSO_4$ and 0.2 M $MnSO_4$ was utilized in XAS to obtain a better signal-to-noise ratio. A 6 mm hole (coin cell Kapton window size) was made in the Zn anode to allow the transmission of X-rays. Galvanostatic cycling tests were conducted using a LANHE M340A cycler at different C-rates with the potential limitations of 0.9–1.8 V *vs.* Zn/Zn^{2+}, 1C = 308 mA g^{-1}. *Operando* XAS tests were conducted using a BioLogic VSP potentiostat, and *in situ* STXM using a BioLogic SP-200 potentiostat.

Material characterization

XRD patterns were collected by a Siemens D-5000 diffractometer of Cu Kα radiation. *Operando* XRD data were acquired by a Bruker D8 Advance A25 diffractometer in a Debye–Scherrer geometry equipped with a Johansson monochromator of the Mo Kα radiation and its standard transmission diffraction collection mode. Scanning electron microscopy (SEM) was performed using a FEI Quanta 200 FEG-ESEM equipment (10–15 kV). XPS data were recorded by a SPECS EA10P hemispherical analyzer with a monochromatic Al Kα radiation. ICP-OES was taken on samples digested by duplicate in a microwave oven with a mixture of concentrated HNO_3 and HCl solutions. Scanning Transmission electron microscopy (STEM), TEM-EDX and STEM-EELS were acquired with a super-X EDX spectrometer and a Gatan Continuum K3 EELS spectrometer, respectively. Spectra were collected at a beam energy of 200 keV with an energy step of 0.9 eV. Mn K-edge XAS and Mn $K_{\beta 1,3}$ XES experiments were carried out at the CLÆSS beamline of ALBA CELLS synchrotron, Spain.[82,83] *Ex situ* energy-resolved full-field soft TXM was performed at the MISTRAL beamline of ALBA

CELLS synchrotron, Spain.[84] *In situ* scanning X-ray transmission microscopy (STXM) was carried out at the DEMETER beamline of SOLARIS Synchrotron, Poland.[85] The STXM images were obtained at the energy of *ca.* 1010 eV to optimize the compromise between contrast and radiation damage. More details are provided in SI Part I.

XPS fitting was carried out with CasaXPS for Mn $2p_{3/2}$, K 2p, and O 1s lines following the procedure described in our previous report.[56] For XAS techniques, the Zn and Mn mole evolutions in the electrode and electrolyte of the *operando* cell were calculated from the XANES edge jumps with a in-house model detailed in the SI. The EXAFS portion of the *operando* XAS data was analyzed using ATHENA and ARTEMIS.[86,87] For the fitting of the pre-edge, the baseline was modeled with the Larch package.[88] The MnO_2 and Mn_2O_3 reference spectra were taken as models of Mn(IV) and Mn(III) components, respectively, using the Hyperspy package.[89–92] For XES measurements, a linear background was subtracted in SpectroChemPy,[93] considering 0.5–2 eV of the low- and high-energy tails. Subsequently, each spectrum was normalized to its area. The integrated absolute difference (IAD) with respect to a low-spin reference method was utilized to extract the local magnetic moment quantitatively.[94–96] The *ex situ* TXM data were processed following previous work.[59,97,98] *In situ* STXM images and Mn spectra were obtained in aXis2000.[99] (S)TEM-related dataset (HRTEM, STEM-HAADF images, TEM-EDX, and STEM-EELS) were treated with eXSpy.[100] More details are provided in SI Part I.

For big datasets such as *operando* XAS and *ex situ* TXM, linear combination fitting (LCF) was exploited to extract the relative ratios of coexisting components whenever the correct reference set was available. Advanced statistical methods were applied to all large datasets. In particular, principal component analysis (PCA) was performed to determine the maximum number of independent components necessary to reconstruct the information contained in the entire dataset using both MATLAB and the SpectroChemPy package. Finally, multivariate curve resolution-alternating least squares (MCR-ALS) was applied using the MATLAB-based MCR-ALS 2.0 toolbox,[101] to determine physically meaningful spectra and corresponding concentrations.[102,103] For image stack datasets, such as *ex situ* TXM and STEM-EELS, cluster analysis (CA) was applied to determine spatially correlated spectra,[59,104] which was implemented in eXSpy and Hyperspy.[92,100] The pixel analysis in *ex situ* TXM was grouping spectra by shape index between Mn(III) and Mn(IV) features. Additional details are provided in SI Part I.

Author contributions

C. L.: conceptualization, data curation, formal analysis, investigation, methodology, software, validation, visualization, writing – original draft, writing – review & editing. V. M. D.: data curation, formal analysis, investigation, methodology, validation, writing – review & editing. A. P. B.: formal analysis, methodology, writing – review & editing. S. K.: data curation, formal analysis, writing – review & editing. B. M. B.: data curation, formal analysis, validation, writing – review & editing. K. M.: data curation, writing – review & editing. L. S.: formal analysis, funding acquisition, methodology, software, validation, writing – review & editing. A. S.: data curation, formal analysis, funding acquisition, methodology, software, validation, visualization, writing – review & editing. L. S.: conceptualization, data curation, formal analysis, funding acquisition, investigation, methodology, project administration, software, validation, writing – review & editing. D. T.: conceptualization, data curation, formal analysis, funding acquisition, investigation, methodology, project administration, resources, supervision, validation, visualization, writing – review & editing.

Conflicts of interest

There are no conflicts to declare.

Data availability

The data supporting this paper have been included as part of the supplementary information (SI). Supplementary information: experimental details and results. See DOI: **https://doi.org/10.1039/d5ee03588k**.

Raw data and analysis results are available at Zenodo at: **https://doi.org/10.5281/zenodo.17092706**.

Acknowledgements

Cheng Liu is very grateful for financial support from the China Scholarship Council (CSC no.: 202106370079). This study was also implemented within the framework of the doctoral program in Materials Science at the Universitat Autònoma de Barcelona (UAB, Spain). This research was funded by the Spanish Agency for Research (AEI) co-funded with ERDF through the ''Severo Ochoa'' Programme for Centers of Excellence in R&D (CEX2023-001263-S) and the projects PID2021-124681OB-I00 and TED2021-132707B-I00. This research was partially developed within the CSIC Interdisciplinary Thematic Platform PTI-TRANSENER+ as part of the CSIC programme for the Spanish Recovery, Transformation, and Resilience Plan funded by the Recovery and Resilience Facility of the European Union, established by Regulation (EU) 2020/2094. Coding support for Hyperspy, eXSpy, and SpectroChemPy from the respective communities and, in particular, assistance from licouplings@gmail.com and yezhihang@live.com is warmly acknowledged. Material suggestions and synthesis help from Wenhai Wang and Canhuang Li are warmly appreciated. We thank Anna Esther Carrillo, and Judith Oró Solé in the Service at the ICMAB for arrangements of SEM and TEM sessions. Synchrotron-based measurements were performed at CLÆSS and MISTRAL, of ALBA CELLS Synchrotron with the collaboration of ALBA staff. Authors acknowledge the use of instrumentation, as well as the technical advice provided by the Joint Electron Microscopy Center at ALBA (JEMCA) and funding

from Grant IU16-014206 (METCAM–FIB) to ICN2 funded by the European Union through the European Regional Development Fund (ERDF), with the support of the Ministry of Research and Universities, Generalitat de Catalunya. This publication was partially developed under the provision of the Polish Ministry of Science and Higher Education project "Support for research and development with the use of research infra-structure of the National Synchrotron Radiation Centre SOLARIS" under contract no 1/SOL/2021/2. Lorenzo Stievano gratefully acknowledges financial support from the French National Research Agency (project Labex STORE-EX, ANR-10-LABX-76-01).

Notes and references

1 J. Amici, P. Asinari, E. Ayerbe, P. Barboux, P. Bayle-Guillemaud, R. J. Behm, M. Berecibar, E. Berg, A. Bhowmik, S. Bodoardo, I. E. Castelli, I. Cekic-Laskovic, R. Christensen, S. Clark, R. Diehm, R. Dominko, M. Fichtner, A. A. Franco, A. Grimaud, N. Guillet, M. Hahlin, S. Hartmann, V. Heiries, K. Hermansson, A. Heuer, S. Jana, L. Jabbour, J. Kallo, A. Latz, H. Lorrmann, O. M. Løvvik, S. Lyonnard, M. Meeus, E. Paillard, S. Perraud, T. Placke, C. Punckt, O. Raccurt, J. Ruhland, E. Sheridan, H. Stein, J. Tarascon, V. Trapp, T. Vegge, M. Weil, W. Wenzel, M. Winter, A. Wolf and K. Edström, *Adv. Energy Mater.*, 2022, **12**, 2102785.
2 Z. Zhu, T. Jiang, M. Ali, Y. Meng, Y. Jin, Y. Cui and W. Chen, *Chem. Rev.*, 2022, **122**, 16610–16751.
3 S. Chu and A. Majumdar, *Nature*, 2012, **488**, 294–303.
4 S. W. D. Gourley, R. Brown, B. D. Adams and D. Higgins, *Joule*, 2023, **7**, 1415–1436.
5 L. E. Blanc, D. Kundu and L. F. Nazar, *Joule*, 2020, **4**, 771–799.
6 A. Innocenti, D. Bresser, J. Garche and S. Passerini, *Nat. Commun.*, 2024, **15**, 4068.
7 T. Yamamoto and T. Shoji, *Inorg. Chim. Acta*, 1986, **117**, L27–L28.
8 B. Sambandam, V. Mathew, S. Kim, S. Lee, S. Kim, J. Y. Hwang, H. J. Fan and J. Kim, *Chem*, 2022, **8**, 924–946.
9 L. Tang, H. Peng, J. Kang, H. Chen, M. Zhang, Y. Liu, D. H. Kim, Y. Liu and Z. Lin, *Chem. Soc. Rev.*, 2024, **53**, 4877–4925.
10 Y. Ren, H. Li, Y. Rao, H. Zhou and S. Guo, *Energy Environ. Sci.*, 2024, **17**, 425–441.
11 T. A. Zordan and L. G. Hepler, *Chem. Rev.*, 1968, **68**, 737–745.
12 A. Era, Z. Takehara and S. Yoshizawa, *Electrochim. Acta*, 1967, **12**, 1199–1212.
13 B. Lee, C. S. Yoon, H. R. Lee, K. Y. Chung, B. W. Cho and S. H. Oh, *Sci. Rep.*, 2014, **4**, 6066.
14 C. Xu, B. Li, H. Du and F. Kang, *Angew. Chem., Int. Ed.*, 2012, **51**, 933–935.
15 M. H. Alfaruqi, V. Mathew, J. Gim, S. Kim, J. Song, J. P. Baboo, S. H. Choi and J. Kim, *Chem. Mater.*, 2015, **27**, 3609–3620.
16 N. Zhang, F. Cheng, J. Liu, L. Wang, X. Long, X. Liu, F. Li and J. Chen, *Nat. Commun.*, 2017, **8**, 405.
17 T. Shoji and T. Yamamoto, *J. Electroanal. Chem.*, 1993, **362**, 153–157.
18 B. Lee, H. R. Lee, H. Kim, K. Y. Chung, B. W. Cho and S. H. Oh, *Chem. Commun.*, 2015, **51**, 9265–9268.
19 H. Pan, Y. Shao, P. Yan, Y. Cheng, K. S. Han, Z. Nie, C. Wang, J. Yang, X. Li, P. Bhattacharya, K. T. Mueller and J. Liu, *Nat. Energy*, 2016, **1**, 16039.
20 P. Oberholzer, E. Tervoort, A. Bouzid, A. Pasquarello and D. Kundu, *ACS Appl. Mater. Interfaces*, 2019, **11**, 674–682.
21 Y. Yuan, R. Sharpe, K. He, C. Li, M. T. Saray, T. Liu, W. Yao, M. Cheng, H. Jin, S. Wang, K. Amine, R. Shahbazian-Yassar, M. S. Islam and J. Lu, *Nat. Sustain.*, 2022, **5**, 890–898.
22 X. Ye, D. Han, G. Jiang, C. Cui, Y. Guo, Y. Wang, Z. Zhang, Z. Weng and Q.-H. Yang, *Energy Environ. Sci.*, 2023, **16**, 1016–1023.
23 B. Lee, H. R. Seo, H. R. Lee, C. S. Yoon, J. H. Kim, K. Y. Chung, B. W. Cho and S. H. Oh, *ChemSusChem*, 2016, **9**, 2948–2956.
24 M. Chamoun, W. R. Brant, C.-W. Tai, G. Karlsson and D. Noréus, *Energy Storage Mater.*, 2018, **15**, 351–360.
25 C. F. Bischoff, O. S. Fitz, J. Burns, M. Bauer, H. Gentischer, K. P. Birke, H.-M. Henning and D. Biro, *J. Electrochem. Soc.*, 2020, **167**, 020545.
26 X. Gao, H. Wu, W. Li, Y. Tian, Y. Zhang, H. Wu, L. Yang, G. Zou, H. Hou and X. Ji, *Small*, 2020, **16**, 1905842.
27 Y. Li, S. Wang, J. R. Salvador, J. Wu, B. Liu, W. Yang, J. Yang, W. Zhang, J. Liu and J. Yang, *Chem. Mater.*, 2019, **31**, 2036–2047.
28 S. Cui, D. Zhang and Y. Gan, *Adv. Energy Mater.*, 2024, **14**, 2302655.
29 L. Wu, Z. Li, Y. Xiang, W. Dong, X. Qi, Z. Ling, Y. Xu, H. Wu, M. D. Levi, N. Shpigel and X. Zhang, *Small*, 2024, **20**, 2404583.
30 D. Wu, L. M. Housel, S. T. King, Z. R. Mansley, N. Sadique, Y. Zhu, L. Ma, S. N. Ehrlich, H. Zhong, E. S. Takeuchi, A. C. Marschilok, D. C. Bock, L. Wang and K. J. Takeuchi, *J. Am. Chem. Soc.*, 2022, **144**, 23405–23420.
31 V. R. Kankanallu, X. Zheng, D. Leschev, N. Zmich, C. Clark, C.-H. Lin, H. Zhong, S. Ghose, A. M. Kiss, D. Nykypanchuk, E. Stavitski, E. S. Takeuchi, A. C. Marschilok, K. J. Takeuchi, J. Bai, M. Ge and Y. K. Chen-Wiegart, *Energy Environ. Sci.*, 2023, **16**, 2464–2482.
32 H. Moon, K. Ha, Y. Park, J. Lee, M. Kwon, J. Lim, M. Lee, D. Kim, J. H. Choi, J. Choi and K. T. Lee, *Adv. Sci.*, 2021, **8**, 2003714.
33 D. Wu, L. M. Housel, S. J. Kim, N. Sadique, C. D. Quilty, L. Wu, R. Tappero, S. L. Nicholas, S. Ehrlich, Y. Zhu, A. C. Marschilok, E. S. Takeuchi, D. C. Bock and K. J. Takeuchi, *Energy Environ. Sci.*, 2020, **13**, 4322–4333.
34 T.-H. Wu, Y.-Q. Lin, Z. D. Althouse and N. Liu, *ACS Appl. Energy Mater.*, 2021, **4**, 12267–12274.
35 Q. Duan, Y. Zheng, Y. Zhou, S. Dong, C. Ku, P. H.-L. Sit and D. Y. W. Yu, *Small*, 2024, **20**, 2404368.

36 Y. Chen, C. Lin, X. Chen, Z. Lu, K. Zhang, Y. Liu, J. Wang, G. Han and G. Xu, *Adv. Energy Mater.*, 2024, **14**, 2304303.
37 G. Cui, Y. Zeng, J. Wu, Y. Guo, X. Gu and X. W. (David), Lou, *Adv. Sci.*, 2022, **9**, 2106067.
38 F. Zhao, J. Li, A. Chutia, L. Liu, L. Kang, F. Lai, H. Dong, X. Gao, Y. Tan, T. Liu, I. P. Parkin and G. He, *Energy Environ. Sci.*, 2024, **17**, 1497–1508.
39 X. Zhang, J. Li, H. Ao, D. Liu, L. Shi, C. Wang, Y. Zhu and Y. Qian, *Energy Storage Mater.*, 2020, **30**, 337–345.
40 F. Wan, R. Liu, Y. Xia, K. Hu, Y. Lei, C. Wang, S. Zhang, S. Li, D. Yang, Y. Zheng and W. Chen, *Inorg. Chem.*, 2024, **63**, 6988–6997.
41 T. Shoji, M. Hishinuma and T. Yamamoto, *J. Appl. Electrochem.*, 1988, **18**, 521–526.
42 Y. Xiong, Y. Kong, L. Xu, H. Li, Y. Zhong, B. He, M. Wang, L. Jin, W. Lu and H. Wang, *J. Energy Storage*, 2024, **97**, 112985.
43 X. Xiao, L. Zhang, W. Xin, M. Yang, Y. Geng, M. Niu, H. Zhang and Z. Zhu, *Small*, 2024, **20**, 2309271.
44 J. T. Simon, V. Šedajová, D. Tripathy, H. E. Smith, S. M. Clarke, C. P. Grey and S. Menkin, *J. Mater. Chem. A*, 2024, **12**, 24916–24933.
45 W. Sun, F. Wang, S. Hou, C. Yang, X. Fan, Z. Ma, T. Gao, F. Han, R. Hu, M. Zhu and C. Wang, *J. Am. Chem. Soc.*, 2017, **139**, 9775–9778.
46 X. Guo, J. Zhou, C. Bai, X. Li, G. Fang and S. Liang, *Mater. Today Energy*, 2020, **16**, 100396.
47 G. Li, W. Chen, H. Zhang, Y. Gong, F. Shi, J. Wang, R. Zhang, G. Chen, Y. Jin, T. Wu, Z. Tang and Y. Cui, *Adv. Energy Mater.*, 2020, **10**, 1902085.
48 X. Zeng, J. Liu, J. Mao, J. Hao, Z. Wang, S. Zhou, C. D. Ling and Z. Guo, *Adv. Energy Mater.*, 2020, **10**, 1904163.
49 M. Mateos, N. Makivic, Y. Kim, B. Limoges and V. Balland, *Adv. Energy Mater.*, 2020, **10**, 2000332.
50 J. C. Bernard, Z. Wang, S. Yan, E. S. Takeuchi, A. C. Marschilok, K. J. Takeuchi and A. C. West, *J. Electrochem. Soc.*, 2024, **171**, 050502.
51 Y. Li, Y. Li, Q. Liu, Y. Liu, T. Wang, M. Cui, Y. Ding, H. Li and G. Yu, *Angew. Chem., Int. Ed.*, 2024, **63**, e202318444.
52 L. Godeffroy, I. Aguilar, J. Médard, D. Larcher, J. Tarascon and F. Kanoufi, *Adv. Energy Mater.*, 2022, **12**, 2200722.
53 E. Andreoli, D. A. Rooney, W. Redington, R. Gunning and C. B. Breslin, *J. Nanosci. Nanotechnol.*, 2012, **12**, 338–349.
54 N. J. Herrmann, H. Euchner, A. Groß and B. Horstmann, *Adv. Energy Mater.*, 2024, **14**, 2302553.
55 J. Pross-Brakhage, J. Meyer, C. Mehlich, O. Fitz and P. Birke, *J. Electrochem. Soc.*, 2025, **172**, 050513.
56 M. C. Biesinger, B. P. Payne, A. P. Grosvenor, L. W. M. Lau, A. R. Gerson, R. St. and C. Smart, *Appl. Surf. Sci.*, 2011, **257**, 2717–2730.
57 B. Gilbert, B. H. Frazer, A. Belz, P. G. Conrad, K. H. Nealson, D. Haskel, J. C. Lang, G. Srajer and G. De Stasio, *J. Phys. Chem. A*, 2003, **107**, 2839–2847.
58 H. Visser, E. Anxolabéhère-Mallart, U. Bergmann, P. Glatzel, J. H. Robblee, S. P. Cramer, J.-J. Girerd, K. Sauer, M. P. Klein and V. K. Yachandra, *J. Am. Chem. Soc.*, 2001, **123**, 7031–7039.
59 A. Sorrentino, L. Simonelli, A. Kazzazi, N. Laszczynski, A. Birrozzi, A. Mullaliu, E. Pereiro, S. Passerini, M. Giorgetti and D. Tonti, *Appl. Sci.*, 2021, **11**, 2791.
60 H. Tan, J. Verbeeck, A. Abakumov and G. Van Tendeloo, *Ultramicroscopy*, 2012, **116**, 24–33.
61 Q. Zhang, J. Zhao, X. Chen, R. Yang, T. Ying, C. Cheng, B. Liu, J. Fan, S. Li and Z. Zeng, *Adv. Funct. Mater.*, 2024, **34**, 2306652.
62 D. M. Sherman, *Phys. Chem. Miner.*, 1987, **14**, 364–367.
63 E. K. Zimmerer and J. W. Gallaway, *MRS Commun.*, 2025, **15**, 697–704.
64 H. Yan, B. Liu, X. Zhou, F. Meng, M. Zhao, Y. Pan, J. Li, Y. Wu, H. Zhao, Y. Liu, X. Chen, L. Li, X. Feng, D. Chen, H. Shan, C. Yang and N. Yan, *Nat. Commun.*, 2023, **14**, 4509.
65 Y. F. Yao, N. Gupta and H. S. Wroblowa, *J. Electroanal. Chem. Interfacial Electrochem.*, 1987, **223**, 107–117.
66 W. Chen, G. Li, A. Pei, Y. Li, L. Liao, H. Wang, J. Wan, Z. Liang, G. Chen, H. Zhang, J. Wang and Y. Cui, *Nat. Energy*, 2018, **3**, 428–435.
67 M. Mateos, K. D. Harris, B. Limoges and V. Balland, *ACS Appl. Energy Mater.*, 2020, **3**, 7610–7618.
68 J. E. Post and D. R. Veblen, *Am. Mineral.*, 1990, **75**, 477–489.
69 K.-W. Nam, M. G. Kim and K.-B. Kim, *J. Phys. Chem. C*, 2007, **111**, 749–758.
70 L. Chen, Z. Yang, F. Cui, J. Meng, Y. Jiang, J. Long and X. Zeng, *Mater. Chem. Front.*, 2019, **4**, 213–221.
71 J. Ye, P. Li, Z. Hou, W. Zhang, W. Zhu, S. Jin and H. Ji, *Angew. Chem.*, 2024, **136**, e202410900.
72 T. Wang, J. Jin, X. Zhao, X. Qu, L. Jiao and Y. Liu, *Angew. Chem., Int. Ed.*, 2024, **63**, e202412057.
73 Z. Li, Z. Ye, G. Liu, Z. Jiang, W. Jiang, J. Luo, S. Liu, H. Hu, Z. Huang and L. Liu, *Batteries Supercaps*, 2024, e202400660.
74 X. Gao, C. Shen, H. Dong, Y. Dai, P. Jiang, I. P. Parkin, H. Zhang, C. J. Carmalt and G. He, *Energy Environ. Sci.*, 2024, **17**, 2287–2297.
75 Y. Liu, Y. Wang, Y. Ma, X. Zhang, G. Xu and Y. Song, *Small*, 2025, e04484.
76 S. Jin Jun, J. Lee, M.-H. Ryu, M. Lee, J. Lee, H. Kim, K. Yim and K.-N. Jung, *Chem. Eng. J.*, 2024, **497**, 154394.
77 G. Zhang, J. Zhu, L. Lin, Y. Liu, S. Li, Q. Li, X.-X. Liu and X. Sun, *Chem. Sci.*, 2024, **15**, 3545–3551.
78 D. Xie, Y. Wang, L. Tian, H. Huang, J. Sun, D. Kim, J. Zhao and J. Mao, *Adv. Funct. Mater.*, 2025, **35**, 2413993.
79 S. Wang, S. Yao, F. Zhang, K. Ji, Y. Ji, J. Li, W. Fu, Y. Liu, J. Yang, R. Liu, J. Xie, Z. Yang and Y. Yan, *Angew. Chem., Int. Ed.*, 2025, **64**, e202415997.
80 S. J. Kim, D. Wu, N. Sadique, C. D. Quilty, L. Wu, A. C. Marschilok, K. J. Takeuchi, E. S. Takeuchi and Y. Zhu, *Small*, 2020, **16**, 2005406.
81 J. Vicat, E. Fanchon, P. Strobel and D. Tran Qui, *Acta Crystallogr., Sect. B: Struct. Sci.*, 1986, **42**, 162–167.
82 L. Simonelli, C. Marini, L. Ribo, R. Homs, J. Avila, D. Heinis, I. Preda and K. Klementiev, *J. Synchrotron Radiat.*, 2023, **30**, 235–241.
83 L. Simonelli, C. Marini, W. Olszewski, M. Ávila Pérez, N. Ramanan, G. Guilera, V. Cuartero and K. Klementiev, *Cogent Phys.*, 2016, **3**, 1231987.

84 A. Sorrentino, J. Nicolás, R. Valcárcel, F. J. Chichón, M. Rosanes, J. Avila, A. Tkachuk, J. Irwin, S. Ferrer and E. Pereiro, *J. Synchrotron Radiat.*, 2015, **22**, 1112–1117.
85 J. Szlachetko, J. Szade, E. Beyer, W. Błachucki, P. Ciochoń, P. Dumas, K. Freindl, G. Gazdowicz, S. Glatt, K. Guła, J. Hormes, P. Indyka, A. Klonecka, J. Kołodziej, T. Kołodziej, J. Korecki, P. Korecki, F. Kosiorowski, K. Kosowska, G. Kowalski, M. Kozak, P. Kozioł, W. Kwiatek, D. Liberda, H. Lichtenberg, E. Madej, A. Mandziak, A. Marendziak, K. Matlak, A. Maximenko, P. Nita, N. Olszowska, R. Panaś, E. Partyka-Jankowska, M. Piszak, A. Prange, M. Rawski, M. Roman, M. Rosmus, M. Sikora, J. Sławek, T. Sobol, K. Sowa, N. Spiridis, J. Stępień, M. Szczepanik, M. Ślęzak, T. Ślęzak, T. Tyliszczak, G. Ważny, J. Wiechecki, D. Wilgocka-Ślęzak, B. Wolanin, P. Wróbel, T. Wróbel, M. Zając, A. Wawrzyniak and M. Stankiewicz, *Eur. Phys. J. Plus*, 2023, **138**, 10.
86 B. Ravel and M. Newville, *J. Synchrotron Radiat.*, 2005, **12**, 537–541.
87 M. Newville, *J. Synchrotron Radiat.*, 2001, **8**, 96–100.
88 M. Newville, *J. Phys.: Conf. Ser.*, 2013, **430**, 012007.
89 F. Farges, *Phys. Rev. B: Condens. Matter Mater. Phys.*, 2005, **71**, 155109.
90 E. Chalmin, F. Farges and G. E. Brown, *Contrib. Mineral. Petrol.*, 2009, **157**, 111–126.
91 F. Farges, Y. Lefrère, S. Rossano, A. Berthereau, G. Calas and G. E. Brown, *J. Non-Cryst. Solids*, 2004, **344**, 176–188.
92 F. de la Peña, E. Prestat, J. Lähnemann, V. T. Fauske, P. Burdet, P. Jokubauskas, T. Furnival, C. Francis, M. Nord, T. Ostasevicius, K. E. MacArthur, D. N. Johnstone, M. Sarahan, J. Taillon, T. Aarholt, Pquinn-Dls, V. Migunov, A. Eljarrat, J. Caron, T. Nemoto, T. Poon, S. Mazzucco, Sivborg, Actions-User, N. Tappy, N. Cautaerts, S. Somnath, T. Slater, M. Walls and Pietsjoh, *hyperspy/hyperspy Zenodo*, 2025.
93 A. Travert and C. Fernandez, *SpectroChemPy, a framework for processing, analyzing and modeling spectroscopic data for chemistry with python (version 0.8.1) Zenodo*, 2025.
94 K. Tsutsumi, H. Nakamori and K. Ichikawa, *Phys. Rev. B*, 1976, **13**, 929–933.
95 G. Vankó, T. Neisius, G. Molnár, F. Renz, S. Kárpáti, A. Shukla and F. M. F. de Groot, *J. Phys. Chem. B*, 2006, **110**, 11647–11653.
96 M. Rovezzi and P. Glatzel, *Semicond. Sci. Technol.*, 2014, **29**, 023002.
97 L. Simonelli, A. Sorrentino, C. Marini, N. Ramanan, D. Heinis, W. Olszewski, A. Mullaliu, A. Birrozzi, N. Laszczynski, M. Giorgetti, S. Passerini and D. Tonti, *J. Phys. Chem. Lett.*, 2019, **10**, 3359–3368.
98 S. E. Ali, W. Olszewski, A. Sorrentino, C. Marini, A. Kazzazi, N. Laszczynski, A. Birrozzi, A. Mullaliu, S. Passerini, D. Tonti and L. Simonelli, *J. Phys. Chem. Lett.*, 2021, **12**, 1195–1201.
99 A. P. Hitchcock, *J. Electron Spectrosc. Relat. Phenom.*, 2023, **266**, 147360.
100 F. de la Peña, E. Prestat, P. Burdet, J. Lähnemann, K. E. MacArthur, V. T. Fauske, M. Sarahan, C. Francis, D. N. Johnstone, T. Ostasevicius, V. Migunov, T. Furnival, M. Nord, S. Mazzucco, A. Eljarrat, J. Caron, T. Aarholt, T. Poon, Z. Zhang, P. Jokubauskas, Actions-User, F. Winkler, J. Taillon, T. Slater, Pquinn-Dls, G. Guzzinati, J. C. Myers and N. Tappy, *hyperspy/exspy Zenodo*, 2025.
101 J. Jaumot, A. De Juan and R. Tauler, *Chemom. Intell. Lab. Syst.*, 2015, **140**, 1–12.
102 R. Tauler and A. de Juan, in *Data Handling in Science and Technology*, ed. A. M. de la Peña, H. C. Goicoechea, G. M. Escandar and A. C. Olivieri, Elsevier, 2015, vol. 29, pp. 247–292, DOI: **10.1016/B978-0-444-63527-3.00005-9**.
103 J. M. Amigo, A. De Juan, J. Coello and S. Maspoch, *Anal. Chim. Acta*, 2006, **567**, 236–244.
104 M. Lerotic, C. Jacobsen, T. Schäfer and S. Vogt, *Ultramicroscopy*, 2004, **100**, 35–57.

